nature communications

Article

https://doi.org/10.1038/s41467-025-56802-0

Fast autoxidation of unsaturated lipid films on indoor surfaces

Received: 27 September 2024

Accepted: 31 January 2025

Xinke Wang, William D. Fahy, Linna Xie, Hui Peng & Jonathan P. D. Abbatt

Organic films containing unsaturated lipids are widespread, yet their oxidation pathways with associated impacts on contaminant lifetimes and human exposure remain poorly explored under indoor environmental conditions. This study demonstrates that UVA radiation and radical exposure drive rapid autoxidation of thin films of methyl linolenate (ML) and canola oil (which contains polyunsaturated triglycerides), primarily producing organic hydroperoxides. For ML films this fast chemistry occurs at the same rate under entirely dark, genuine indoor conditions as it does when the films are exposed to significantly higher $^{\bullet}$OH radicals in a flow reactor. Both $^{\bullet}$OH and organic radicals are detected within the oxidized films, propagating fast autoxidation in dark indoor environments with minimal sensitivity to the radical initiation rate. When mixed into the films, bisphenol A is hydroxylated, illustrating potential transformation pathways for toxic organic contaminants. This study uncovers insights into lipid autoxidation processes under environmental conditions and underscores their potential health impacts.

Autoxidation via H-shift chemistry of peroxy radicals is pivotal in organic oxidation[1–3] across various scientific disciplines. In atmospheric chemistry, autoxidation contributes to the formation of secondary organic aerosols (SOAs)[4–7], impacting air quality and climate. Autoxidation is also a major factor in the degradation of liquid fats and oils, leading to rancidity[8]. In biological systems, autoxidation of lipids is involved in the oxidative stress response[9], leading to reactive oxygen species (ROS) generation associated with cell damage and various diseases, such as cancer[10], atherosclerosis[11], neurodegenerative disorders[12], etc.[3,13] Understanding the mechanisms and kinetics of autoxidation is therefore important for fields ranging from environmental science to health and materials science.

Organic films which contain unsaturated lipids are commonly found in various environments, such as the surfaces of indoors,[14] natural waters[15,16], wax plant surfaces[17], and soil organic coatings[18]. In particular, organic films accumulate on indoor surfaces in the built environment, primarily through the emission and deposition of semivolatile organic compounds from human activities and consumer products[14,19–21]. A notable example is the formation of cooking oil residues on kitchen surfaces, which mainly comprises unsaturated triglycerides[22,23]. Furthermore, unsaturated lipids are a major component of human skin oil[24,25] which is known to widely contaminate indoor spaces.

These unsaturated lipids can react with ozone, producing secondary ozonides (SOZs), organic hydroperoxides (ROOHs) and other products[26–30]. ROS, especially radicals, can initiate lipid autoxidation by abstracting hydrogen atoms from allylic and bis-allylic carbons, generating ROOHs[31,32]. Another mechanism involves the addition of hydroxyl radicals ($^{\bullet}$OH) to C = C bonds leading to formation of Criegee intermediates that drive chain reactions[33,34]. Despite the widespread presence of organic films containing these unsaturated lipids, their oxidation mechanisms under environmental ambient conditions remain poorly explored.

The chemistry of indoor contaminated surfaces is of importance to human health, with the surfaces providing a medium for non-dietary chemical exposure via dermal uptake and non-dietary ingestion mechanisms[35,36]. The partitioning volume of indoor surfaces is so large that all semi- and low-volatility organic contaminants—which includes classes of species with toxic properties, such as PAHs, flame retardants and plasticizers—exist predominantly in these surface reservoirs.

Department of Chemistry, University of Toronto, Toronto, Ontario, Canada. e-mail: jonathan.abbatt@utoronto.ca

Understanding the reactive nature of such organic films and other surface reservoirs is critically important.

We have investigated the detailed chemistry of the autoxidation of polyunsaturated lipid films in the form of both a single compound (methyl linolenate) and a complex mixture of unsaturated triglycerides (in canola cooking oil), to achieve the comprehensive understanding of how such molecules chemically oxidize under genuine indoor conditions. A summary of all experiments is provided in Supplementary Table 1. Major reaction intermediates, including ROS, were identified under both irradiated and dark indoor conditions. Notably, ˙OH radical formation was observed and quantified in the films using a radical trapping probe, while total ROOHs, key products, were measured using two chemical assays. We also found that a common toxic organic contaminant (bisphenol A) is chemically transformed when mixed with aging organic films. Finally, we used a simple kinetic model to demonstrate that these autoxidation processes are sustained by internal radical propagation and not by radical initiation processes, enabling them to proceed rapidly in indoor environments which are known to have low radical abundance. In particular, the goal of this paper is not to demonstrate that autoxidation occurs in organic condensed phases, which has been previously demonstrated[3,37], but rather to determine whether such chemistry occurs sufficiently rapidly that it is important under indoor environmental conditions.

Results

Cooking oil film oxidation

Canola cooking oil films were deposited onto clean Petri dishes and exposed to two distinct environments: (1) a flow reactor under irradiation and (2) a dark indoor environment, specifically inside a desk drawer exposed to ambient office air. The average ozone mixing ratio inside the desk drawer was approximately 12 ppb during the oil film experiment. Figure 1a displays the ESI(+)-MS mass spectra of fresh and irradiated cooking oil films, as well as the oxidized film in the dark indoor environment. Cooking oils consist of a complex mixture of unsaturated triglycerides, with seven major constituents identified here. For example, triolein, at *m/z* 903 $[C_{57}H_{104}O_6 + NH_4]^+$, a triglyceride with three oleate chains [denoted as TG(54:3), where "54" represents the total carbon number of the side chains and "3" indicates the number of C = C bonds], shows the highest signals in the cooking oil. TG(54:6), containing one oleate, one linoleate, and one linolenate chain, is another significant component. TG(54:4), TG(54:5), TG(52:2), TG(52:3), and TG(52:4) are also present in high abundances (Fig. 1a). After irradiation in the flow reactor or oxidation in the dark indoor environment, oxygenated products with up to ten additional oxygen atoms were detected in the cooking oil films (Fig. 1a and Supplementary Table 2). Products with two additional oxygens were particularly abundant.

To confirm the structures of these oxygenated products, a selective MS/MS method for organic hydroperoxide identification was used[27]. As shown in Fig. 1b, products with two, three, and four additional oxygens, exhibiting a neutral loss scan of 51 Da $(H_2O_2 + NH_3)$, were identified as ROOHs[27,38]. More highly oxygenated products were not detected probably due to their low intensities. Figure 1c shows that UVA light exposure causes an initially gradual then sharp increase in ROOH levels in cooking oil films, as measured by the FOX2 assay. This indicates that ROS accumulation accelerates autoxidation. Control experiments showed no ROOH formation (Supplementary Fig. 1). The UVA light intensity was similar to that measured 1 m away from a south-

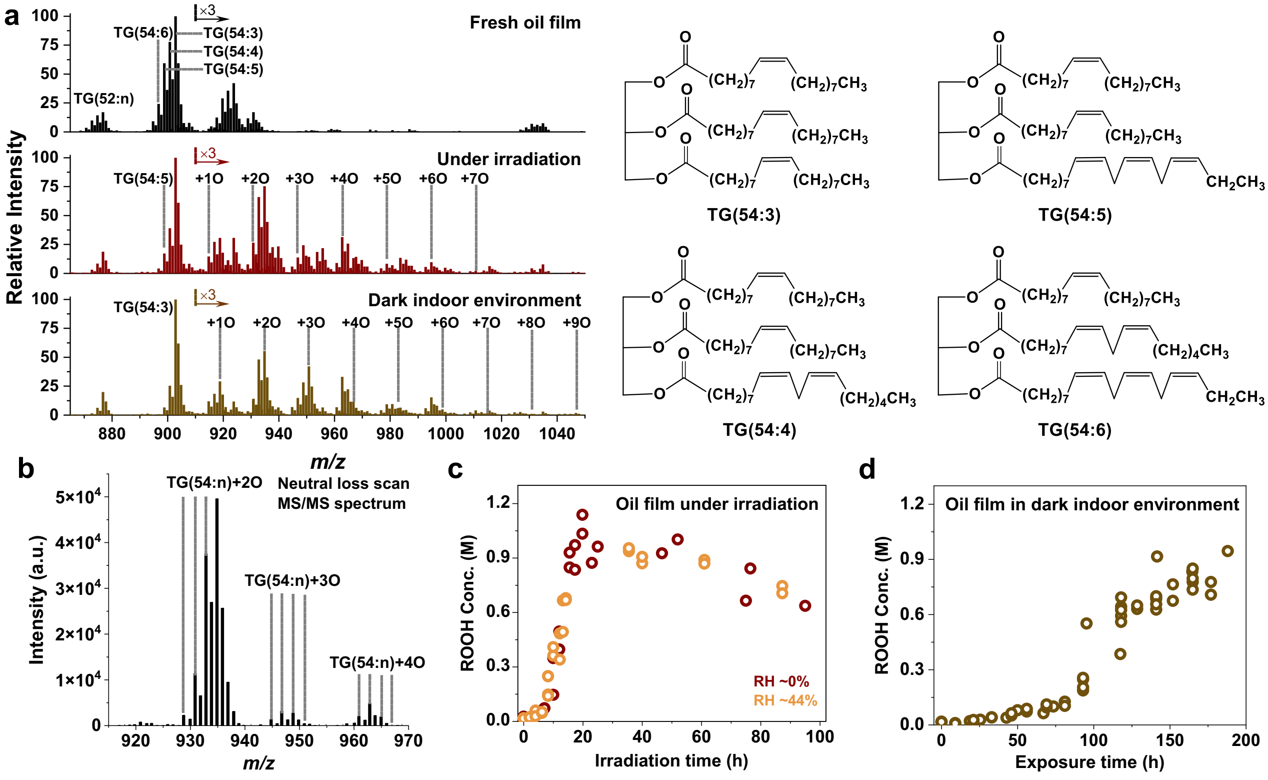

Fig. 1 | Chemical characteristics of oxidized cooking oil films. a Direct infusion ESI(+)-Orbitrap-MS spectra of fresh cooking oil film, film irradiated for 21 h in the flow reactor or aged in the dark indoor environment for 4 days. The intensity of ions with *m/z* > 910 was multiplied by 3. TG(52:n), *n* = 2, 3, 4. For this figure and others in the paper, note that +1 O, +2 O, … refer to the additions of 1, 2, … oxygen atoms to the reactant molecule. **b** TSQ Endura neutral loss scan MS/MS spectrum of indoor aged oil film (5.9 days). TG(54:n), *n* = 3, 4, 5, 6. The peaks were identified as ROOH ions due to a neutral loss of 51 Da $(H_2O_2 + NH_3)$[27,38]. **c**, **d**, Concentration time profiles of ROOH formed from cooking oil films under irradiation in the flow reactor or placement in the dark indoor environment. Source data are provided as a Source Data file.

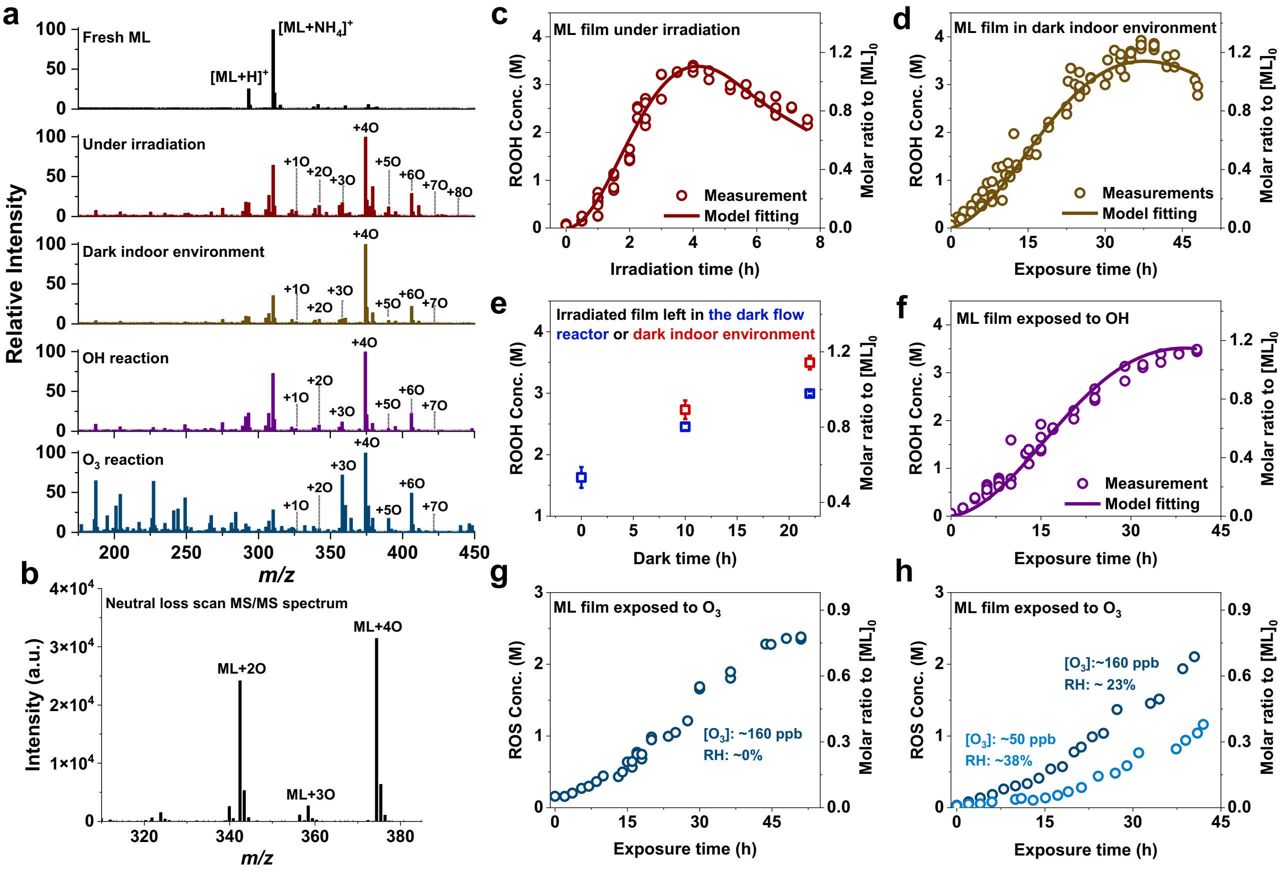

Fig. 2 | Chemical characteristics of oxidized ML films and modeling fittings. **a** Direct infusion ESI(+)-Orbitrap-MS spectra of fresh ML film, film irradiated for 3 h in the flow reactor, aged in the dark environment for 23 h, oxidized by $^{\bullet}OH$ (~1 ppt, Relative Humidity ~22%) for 24 h and oxidized by O_3 (~160 ppb) for 42 h (Relative Humidity ~38%). **b** TSQ Endura neutral loss scan MS/MS spectrum of ML film aged for 17 h in dark indoors. The peaks were identified as ROOH ions. **c**, **d** Concentration time profiles of ROOH formed from ML films under irradiation (Relative Humidity ~38%) and aging in dark indoors. The right Y axis indicates the molar ratio of formed ROS to the original concentration of ML ($[ML]_0$). **e** The variation of ROOH concentration of the irradiated film left in the dark flow reactor (blue) or in the dark indoor environment (red). All error bars in this and other figures denote the standard deviations calculated from experimental replicates. **f**–**h** Concentration time profiles of ROOH or ROS formed from ML films exposed to gaseous $^{\bullet}OH$ radicals or ozone. The model fits in Figs (**c**, **d** and **f**) were based on the kinetics modeling shown in Fig. 4. Source data are provided as a Source Data file.

facing window (Supplementary Fig. 2)[39]. In addition, experiments with varying cooking oil thicknesses under irradiation showed nearly identical ROOH formation profiles, reaching concentrations of about 1 M (Supplementary Fig. 3a). Note that in addition to the FOX2 assay which can detect a few species other than ROOHs, the NPBA assay, known for its selective sensitivity to H_2O_2 and ROOHs[40–42], was also employed to confirm the formation of ROOHs (Supplementary Figs. 3b, c and 4).

A slower autoxidation process was observed when the films were placed in a dark indoor environment. This slower rate is likely due to the relative stability of ROOHs in the absence of light, as ROOHs are less prone to decomposition into alkoxy ($RO^{\bullet}$) and $^{\bullet}OH$ radicals, which otherwise accelerate the autoxidation process. Despite the slower rate, the product distribution and maximum production of ROOHs were similar under both irradiation and dark indoor conditions (Fig. 1). This finding indicates that different oxidants present in the dark indoor environment can induce a comparable autoxidation process in cooking oil films, albeit at a slower pace, as observed under UVA light exposure.

Methyl linolenate film oxidation

Due to the complex composition of cooking oils, understanding their oxidation mechanisms is challenging. For this reason, we utilized methyl linolenate (ML), a related polyunsaturated compound known to undergo autoxidation[43,44]. Our results demonstrate that the product distribution for ML under both UVA and dark indoor conditions is similar (Fig. 2a and Supplementary Table 3), with both conditions leading to the formation of ROOHs (Fig. 2b). However, unlike the most abundant product in cooking oil film oxidation, $[M+2O+NH_4]^+$, the predominant product in ML film oxidation is $[ML+4O+NH_4]^+$, which likely contains two hydroperoxide groups. This is probably due to the presence of two bis-allylic sites in ML, where hydrogen atoms are more susceptible to abstraction[3,27,45]. As well, this finding aligns with the higher concentrations of ROOHs observed in ML oxidation (Fig. 2c, d).

Figures 2c, d show the formation of ROOH in ML films under irradiation or in dark indoor environments. While ROOH formation is significantly faster under irradiation, the maximum production levels are similar. Additionally, ROOH production was not dependent on relative humidity (Fig. 1c and Supplementary Fig. 5). Importantly, Fig. 2e shows that ROOH levels continue to increase when the irradiated films were placed in the dark flow reactor without any gaseous oxidants and in the dark indoor environment, with similar ROOH concentrations arising in both cases. This indicates that when ROS levels are sufficiently abundant in the film, these species, rather than gaseous oxidants, dominate the continuing oxidation of the ML.

To further investigate the oxidation of ML films under indoor conditions, within a flow reactor we exposed ML films to gaseous

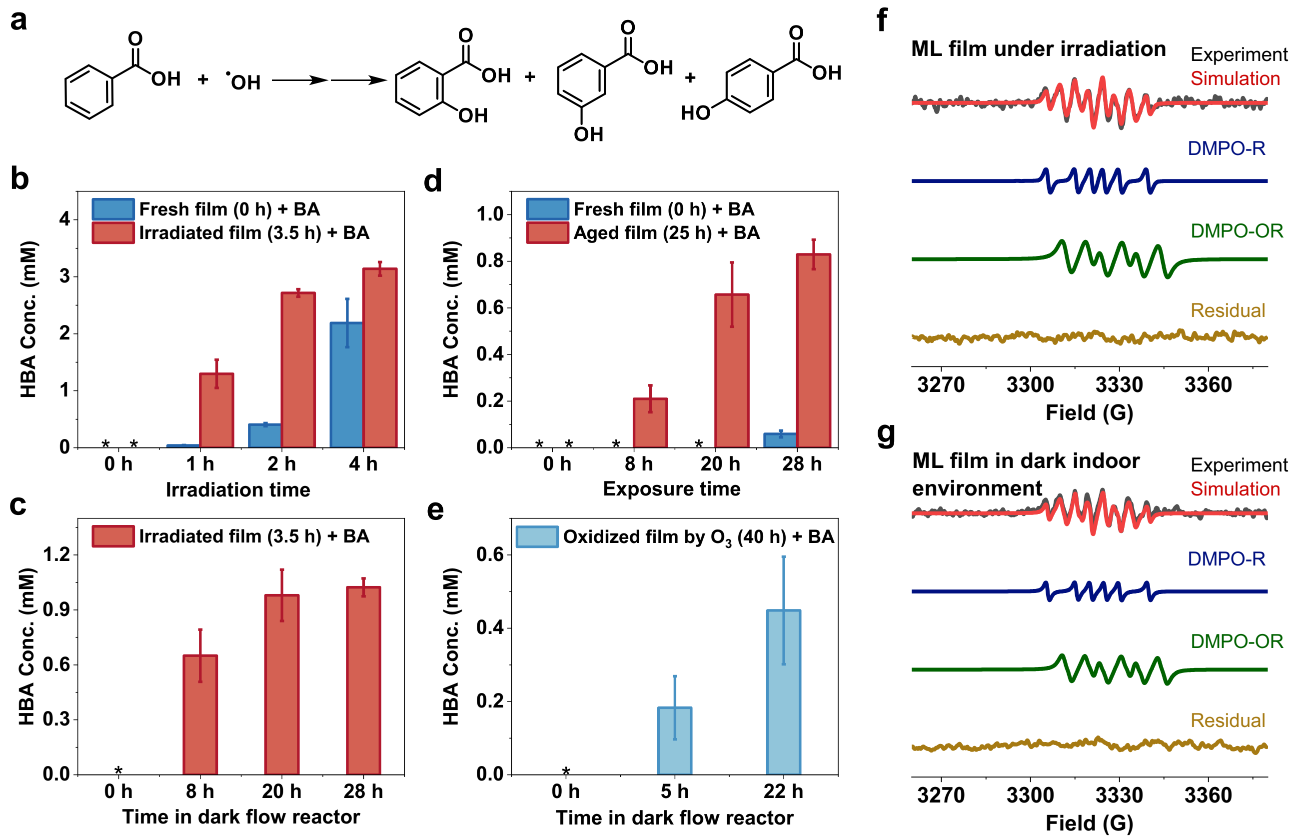

Fig. 3 | Radical measurements. a Mechanism of HBA formation from the reaction of BA with $^{\bullet}$OH radicals. **b**, **c** HBA production over time in fresh or pre-irradiated (3.5 h) ML films with added BA under irradiation or in the dark. **d** HBA production over time in fresh or pre-aged (25 h) ML films with added BA in the dark indoor environment. **e** HBA production over time in oxidized ML films exposed to O_3 (~ 160 ppb, 40 h) with added BA in the dark flow reactor without gaseous oxidants. **f**, **g** Experimentally observed and simulated EPR spectra of ML films under irradiation (5.3 h) or in the dark indoor environment (45.3 h), including deconvolution of the simulation spectrum and residual spectrum (DMPO-R, $a^{N} = \sim14.4$ G, $a^{\beta-H} = \sim 22.0$ G); DMPO-OR, $a^{N} = \sim13.3$ G, $a^{\beta-H} = \sim 8.3$ G, and $a^{\gamma-H} = \sim 1.6$ G). Note that $^{\bullet}$OH and peroxyl radicals were not included in the simulation due to the challenges associated with DMPO spin trapping[27,54,78,79]. Source data are provided as a Source Data file.

ozone, which is believed to be the primary oxidant indoors, and to $^{\bullet}$OH radicals, of which the concentrations indoors are much lower. The product distribution from the reaction of ML with $^{\bullet}$OH radicals closely mirrors that seen in ML films in dark indoor environments (Fig. 2a). In contrast, exposure to ozone leads to a more diverse array of fragmented products. Although products with additional oxygen atoms, such as ROOHs, were also formed from the ML film reaction with ozone, they exhibit a different isomer distribution compared to those formed indoors or from reactions with $^{\bullet}$OH radicals (Supplementary Fig. 6). Besides, SOZs with three additional oxygens are expected to be formed from ML ozonolysis (Supplementary Fig. 6b)[28,46].

In addition, we measured ROOH and ROS formation when ML films were exposed to gaseous $^{\bullet}$OH radicals or ozone, respectively. It should be noted that the FOX2[47,48] and NPBA assays may also be sensitive to SOZs formed from alkene ozonolysis (Supplementary Fig. 7). For clarity, "ROS" was used as the y-axis label in ozonolysis experiments due to the formation of SOZs[28,46]. The time profile of ROOH formation when ML films were exposed to $^{\bullet}$OH radicals closely resembles that in dark indoor environments (Fig. 2d, f). When ML films were exposed to ozone under both dry and humid conditions, ROS production was much lower and slower than in the dark indoor environment, even when ozone mixing ratio reached ~160 ppb (Fig. 2g, h). At lower ozone mixing ratios (~ 50 ppb and ~10 ppb), the ROS concentrations were further reduced. Overall, the similarity in product distribution and the ROOH formation time profile indicates that radicals instead of ozone are primarily responsible for the rapid autoxidation of ML films in the dark indoor environment.

In-film radical measurements

The generation of $^{\bullet}$OH and organic radicals was also observed in films as they chemically oxidized. Benzoic acid (BA) was employed to quantify $^{\bullet}$OH concentrations by quantified observations of 2-, 3-, and 4-hydroxybenzoic acids (HBAs, Fig. 3a)[49,50].

ML films were initially irradiated for 3.5 h in the flow reactor, after which 0.5 mL of BA in a chloroform solution (4 mM) was mixed with the irradiated film. After solvent evaporation, the films were reintroduced into the flow reactor for further irradiation. Fresh ML films with BA were irradiated concurrently for comparison. A significantly higher yield of HBAs was observed in the pre-irradiated films (Fig. 3b). This observation of $^{\bullet}$OH radical generation within organic films complements previous observations of $^{\bullet}$OH generation in SOA extracts, which also contain abundant ROOH molecules[51,52]. HBA formation was also detected when the irradiated films with added BA were left in the dark flow reactor (Fig. 3c). The yield was lower compared to the irradiated conditions, due to the formation of $^{\bullet}$OH radicals from the photolysis of ROOHs under irradiation.

Furthermore, ML films were subjected to a 25-hour oxidation process in the dark indoor environment ("pre-aged" film) before the addition of BA, after which they were left in the dark once more. Fresh films with added BA were also kept in the dark for comparative analysis. The pre-aged films exhibited significantly higher HBA

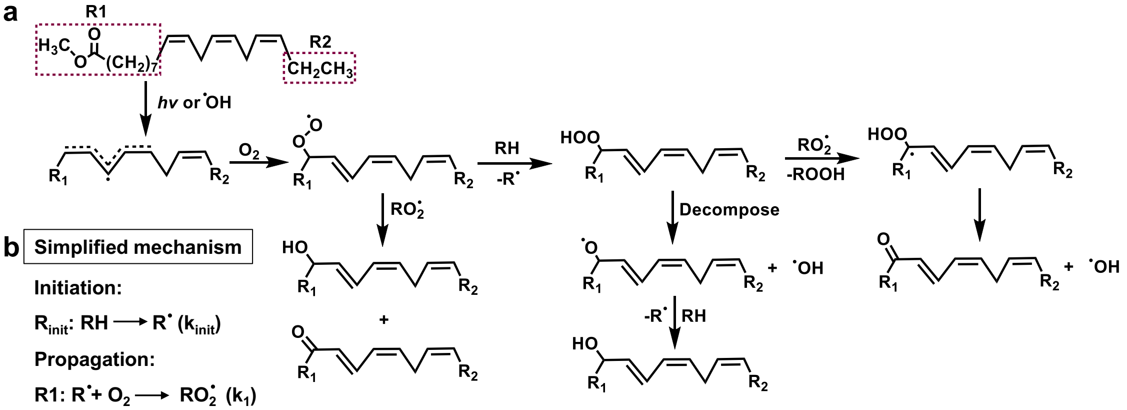

b **Simplified mechanism**

Initiation:

R_{init}: RH ⟶ R˙ (k_{init})

Propagation:

R1: $R^{\bullet} + O_2 \longrightarrow RO_2^{\bullet}$ (k_1)

R2: $RO_2^{\bullet} + RH \longrightarrow ROOH + R^{\bullet}$ (k_2)

R3: $ROOH \longrightarrow RO^{\bullet} + {}^{\bullet}OH$ (k_3)

R4: $RH + {}^{\bullet}OH \longrightarrow R^{\bullet} + H_2O$ (k_4)

Termination:

R5: $RO_2^{\bullet} + RO_2^{\bullet} \longrightarrow ROH + R{=}O$ (k_5)

Other ˙OH sinks:

R6: ${}^{\bullet}OH \longrightarrow$ products (k_6)

c Rate constants for the model fitting

Experiment	k_{init} (s^{-1})	k_1 (s^{-1})	k_2 ($M^{-1}\ s^{-1}$)	k_3 (s^{-1})	k_4 ($M^{-1}\ s^{-1}$)	k_5 ($M^{-1}\ s^{-1}$)	k_6 ($M^{-1}\ s^{-1}$)
Dark indoor environment	$<1.0\times10^{-7}$	1×10^{7}	14	5.0×10^{-6}	1×10^{10}	3.2×10^{7}	1.0×10^{8}
OH oxidation	$<1.0\times10^{-7}$	1×10^{7}	14	4.8×10^{-6}	1×10^{10}	3.2×10^{7}	1.0×10^{8}
Irradiation	$<5.0\times10^{-7}$	1×10^{7}	44	4.9×10^{-5}	1×10^{10}	3.7×10^{7}	1.0×10^{8}

Fig. 4 | Oxidation mechanism and kinetics modeling. a The oxidation mechanism for ML under irradiation or exposure to ˙OH radicals. **b** The simplified model mechanism for ML film oxidation. **c** Rate constants for the model fit. However, note that the model sensitivity to the values of the initiation rate constant can be very low. For example, in the dark indoor environment values of k_{init} from 10^{-20} to $10^{-7}\ s^{-1}$ fit the data well (see Supplementary Fig. 8). For this reason, we list upper limits to the values of k_{init}. The best fit rate constants (units of s^{-1}) were 2.5×10^{-8}, 9.4×10^{-9}, and 8.2×10^{-11}, for the dark indoor environment, OH oxidation, and irradiation experiments, respectively. These values were applied in Fig. 2c, d, and f.

production, reinforcing the evidence for ˙OH radical formation under dark conditions (Fig. 3d). HBAs were also detected in ML films that were first oxidized by ozone for 40 h and then left in the dark flow reactor with added BA (Fig. 3e). However, the HBA concentration was much lower, correlating with reduced ROS production (Fig. 2g, h). The ˙OH radicals formed in the films did not trigger rapid autoxidation in the ozonolysis experiment, likely because the ozone had already consumed a substantial amount of C = C double bonds in the ML film.

Organic radical generation within the oxidized ML films was investigated using electron paramagnetic resonance (EPR) spectroscopy using the spin trapping agent 5,5-dimethyl-1-pyrroline N-oxide (DMPO), commonly used for trapping various radicals, including oxygen-centered, carbon-centered, and nitrogen-centered radicals[27,53,54]. EPR spectral simulation and deconvolution (Fig. 3f, g) indicated the presence of a mixture of carbon-centered alkyl radicals (DMPO-R) and oxygen-centered alkoxyl radicals (DMPO-OR) in the oxidized films. The hyperfine splitting constants derived from these spectra are consistent with values reported in the literature[27,53,54]. These radical species are likely the reactive intermediates in the autoxidation mechanism.

Reaction mechanism and model fitting

Based on prior work in the field[2,3], the proposed mechanism for autoxidation (Fig. 4a) is initiated by light or ˙OH radicals, generating organic alkyl radicals. These radicals react with molecular oxygen to form peroxy radicals, which then undergo hydrogen atom transfer to produce ROOHs and additional organic radicals. This chain reaction propagates free radicals, leading to extensive oxidation of the organic materials.

The time profiles of ROOH formation are strikingly similar during the autoxidation of ML films in dark indoor environments with low oxidant levels (˙OH mixing ratios of 2×10^{-3} - 3×10^{-2} ppt in indoor spaces[55–57], and probably lower in the dark drawer) compared to those in the flow reactor with much higher ˙OH mixing ratios (~1 ppt). In contrast, these profiles differ from those seen in irradiated films. To explore these observations, a kinetics model based on the ML oxidation mechanism was used to simulate ROOH formation (Fig. 4b). More details about the modeling can be found in the "Methods" section, but the important aspects of the model include radical initiation by either photolysis or gas-surface multiphase ˙OH oxidation (R_{init}), propagation (R1-R4), and termination (R5). Since the rate constants for R2 (k_2) and R5 (k_5) are expected to be identical between the dark drawer experiment and flow reactor with elevated ˙OH concentrations, these parameters were fit in the dark drawer experiment and then fixed when fitting the ˙OH flow reactor experiment, which resulted in a similar quality of fit as when k_2 and k_5 were fit in each experiment individually (shown in Supplementary Figs. 8a, b). In addition, R6 is incorporated into the model to simulate other ˙OH sinks within the film.

Given our observations of radical formation and loss of ROOH with time, a key reaction is ROOH decomposition (R3). The detailed mechanism for ROOH decomposition is not known, i.e., whether the peroxide bond is sufficiently weak that it decomposes on the timescale of the observations or whether heterogeneous reactions are involved. Note that to avoid overfitting the model, two ˙OH radicals were generated instead of one RO˙ and one ˙OH from the decomposition of ROOH (R3), as the role of RO˙ is likely analogous to ˙OH under our experimental conditions with high concentrations of bis-allylic hydrogen atoms. A model including hydrogen atom abstraction from ML by RO˙ and both RO˙- RO˙ and RO˙- $RO_2^{\bullet}$ termination steps was constructed, but it was overparameterized, gave similar fit qualities to the existing model, and does not provide any additional insight into the autoxidation mechanism occurring in our experiments.

While this mechanism is highly simplified, it nevertheless demonstrates excellent fits with the ROOH formation time profile observed in both irradiated and dark indoor environments, as well as in

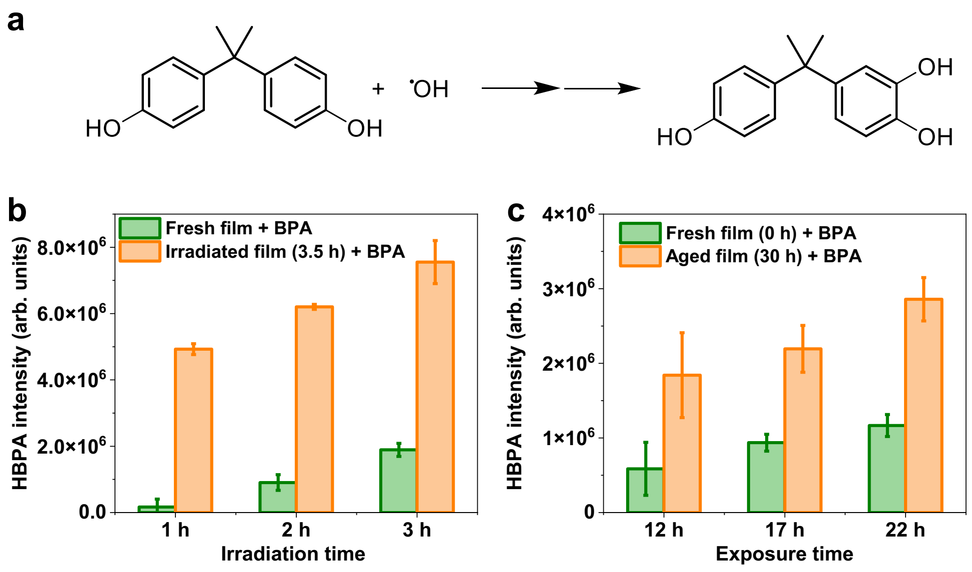

Fig. 5 | BPA decay in oxidized ML films. a Mechanism of HBPA formation from the reaction of BPA with •OH radicals. **b** HBPA production over time in fresh or pre-irradiated (3.5 h) ML films with added BPA under irradiation. **c** HBPA production over time in fresh or pre-aged (30 h) ML films with added BPA in the dark indoor environment. Source data are provided as a Source Data file.

•OH exposure experiments (Fig. 2c, d and f). Notably, we do not need to invoke the addition of •OH radicals to C = C bonds followed by propagation through chain reactions involving Criegee intermediates[34] given the absence of SOZs (Supplementary Fig. 6b) and fragment products (Fig. 2a) in dark indoor environments.

The most important observation in this work is that the kinetics of ROOH formation are the same in the dark indoor environment, with orders of magnitude lower •OH concentrations compared to those in the flow reactor. The model confirms that, aside from k_{init}, the rate constants for R1-R5 in the dark indoor environment and •OH oxidation experiments are similar (see Fig. 4c). The model also demonstrates insensitivity to the value of k_{init}, as values from about $10^{-20}\,s^{-1}$ to $10^{-7}\,s^{-1}$ result in very similar model fits (Supplementary Fig. 8a, b). This indicates that even the low levels of radicals in the dark indoor environment can induce rapid autoxidation of the ML film. This low •OH radical level in the dark indoor environment could be provided by slow gas phase ozonolysis of trace alkenes, or perhaps even by trace transition metals that can induce Fenton chemistry.

Similar model results and model insensitivity for k_{init} were obtained for irradiation of ML, indicating k_{init} is below $5 \times 10^{-7}\,s^{-1}$, which is comparable to the threshold value for dark indoor experiments (Supplementary Fig. 8c). As expected, the rate constant for ROOH decomposition (k_3) is significantly higher in the irradiation case due to photolysis, as compared to the two dark experiments. The value of k_2 is also higher than in the dark experiments (see Fig. 4c), possibly due to differences in the chemical environment of the $RO_2^{\bullet}$ radicals formed following photolytic bond cleavage compared to hydrogen atom abstraction from ML.

Discussion

It is generally assumed that ozone-driven reactions dominate oxidation processes in dark indoor environments[58]. For example, ozone-initiated oxidation of unsaturated films can generate substantial amounts of ROS within the films[48], some of which may be released into the air[59]. However, our findings indicate that a small radical source can initiate the autoxidation of unsaturated lipid films, such as cooking and skin oils. Additionally, our study shows that sunlight irradiation, one meter away from a south-facing window, induces even faster autoxidation compared to indoor gaseous oxidants. This acceleration is likely due to the photolysis of ROOHs, producing RO• and •OH radicals, which propagate radical chemistry. These rapid autoxidation reactions in unsaturated lipid films result in a high yield of ROS, including ROOHs, •OH and oxygenated organic radicals, all of which can substantially impact indoor organic film reactivity and human health.

The large amounts of ROS formed during the oxidation process of unsaturated lipid films can lead to the degradation of indoor organic contaminants. For example, bisphenol A (BPA), a chemical widely used in the manufacture of polycarbonate plastics[60] and known for its endocrine-disrupting effects[61,62], is prevalent in many indoor environments. Our study demonstrates that oxidized lipid films can facilitate the oxidation of BPA, leading to the formation of monohydroxylated BPA (HBPA, see Fig. 5a)[63,64], which exhibits less estrogenic activity than BPA[65,66]. HBPA was observed when fresh or pre-irradiated ML films with added BPA were subjected to irradiation (Fig. 5b). A significantly higher production of HBPA was observed in the pre-irradiated ML films. HBPA formation also occurred when fresh or pre-aged ML films with added BPA were left in a dark indoor environment, with pre-aged films exhibiting higher HBPA levels (Fig. 5c). These results are consistent with experiments involving BA for •OH radical measurement, highlighting the significant role of pre-existing ROS in enhancing further chemical reactions. Given the near-universal ability of •OH to react, we expect that the results demonstrated for BPA would arise with a wide array of organic contaminants.

Overall, this study demonstrates that radical-driven autoxidation processes of organic films that contain unsaturated lipids occur under the dark conditions commonly encountered indoors. The rapid autoxidation process can produce large amounts of ROS (including ROOH, •OH, and RO•), which not only accelerate further autoxidation but also contribute to the oxidation of other contaminants. This reaction is also likely to occur in atmospheric organic aerosols, such as cooking aerosol particles, which account for 11-34% of total organic carbon in polluted urban environments[67,68]. Understanding these mechanisms is important for assessing the impact of unsaturated lipid films and cooking aerosol particles on human health, as the generation of ROS has implications for respiratory and cardiovascular health. As well, this process may contribute to the oxidation of skin oils, due to the presence of reactive unsaturated lipids like arachidonic acid and squalene[25]. This study expands the scope of research on environmental condensed-phase autoxidation processes, offering a foundational understanding of the chemical mechanisms involved.

Methods

Chemicals

All chemicals were used as purchased: methyl linolenate (Sigma-Aldrich, ≥ 99%), chloroform (Sigma-Aldrich, ≥ 99.8%), 1-propanol (Sigma-Aldrich, ≥99.5%), peroxide-free methanol (Fisher, Sequencing Grade), tetramethylethylene (TME, Aldrich, ≥ 99%), isoprene (Aldrich, 99%), tert-butyl hydroperoxide solution (BHPO, Sigma-Aldrich, 70 wt.% in H_2O), xylenol orange tetrasodium salt (Sigma-Aldrich, ACS reagent), ammonium iron(II) sulfate hexahydrate (Sigma-Aldrich, 99%), sulfuric acid (Fisher Scientific, Certified ACS plus), acetic acid (Fisher Scientific, ACS reagent), potassium hydroxide (KOH, Ward's Science, reagent grade), butylated hydroxytoluene (BHT, Millipore Sigma, Certified reference materials), 4-nitrophenylboronic acid (NPBA, Sigma-Aldrich, ≥ 95%), benzoic acid (BA, Sigma-Aldrich, ≥ 99.5%), 2-hydroxybenzoic acid (Thermo scientific, 99%), 3-hydroxybenzoic acid (Sigma-Aldrich, 99%), 4-hydroxybenzoic acid (Sigma-Aldrich, Certified reference materials), ammonium formate (Sigma-Aldrich, ≥ 99%), bisphenol A (BPA, Sigma-Aldrich, ≥ 99%), potassium iodide (KI, Sigma-Aldrich, ≥ 99.99%). The canola oil was sourced from a local retailer in Toronto, ON, Canada[27].

Film preparation and extractions

To prepare the films, 0.5 mL of either ML or canola oil in chloroform solutions with concentrations of 0.1%, 0.05%, and 0.02% (v/v) were pipetted into clean glass Petri dishes. After the solvent fully evaporated, the coatings were immediately placed into the flow reactor or a dark drawer in an office. After the reaction, the oxidized coatings were extracted by 1.5 mL 1-propanol. The extracts were then further diluted for the ROS assays and mass spectrometry analysis.

Flow reactor experiments

The irradiation, ozonolysis, and $^{\bullet}$OH oxidation of organic films were conducted in a cylindrical flow reactor made of quartz (6.5 cm internal diameter and 150 cm length) at room temperature (22-25 °C). Two UVA lamps (SLI Lighting, Germany) positioned above the reactor provided continuous emission ranging from 300 to 420 nm (Supplementary Fig. 2). Airflow rates in the reactor were set to 0.7 L min^{-1} for irradiation, 1.7 L min^{-1} for ozonolysis, and 5 L min^{-1} for $^{\bullet}$OH oxidation experiments. Humidified air was generated by passing zero air (AADCO 737 zero air generator) through a bubbler filled with distilled water (18.2 MΩ cm). An ozone generator comprised of a quartz cell and a Pen-Ray lamp was used to produce ozone by passing 50 mL min^{-1} of zero air through it. A UV photometric ozone analyzer (Thermo Scientific, Model 49 C) and a hygrometer (Vaisala, US) were used to monitor the ozone concentration and Relative Humidity in the outlet of the flow reactor, respectively.

In the $^{\bullet}$OH oxidation experiment, $^{\bullet}$OH radicals were generated by reacting TME (~ 1.9 ppm) with ozone. Ozone mixing ratios declined from about 60 to 43 ppb within the reactor. The TME flow was maintained using a glass diffusion cell (VICI Metronics, USA) at room temperature (~ 295 K). To quantify the $^{\bullet}$OH concentration, a mixture of TME and isoprene in a 90:10 ratio was used in the diffusion cell in a separate experiment. A Vocus 2 R Proton Transfer Reaction Time of Flight Mass Spectrometer (PTR-ToF-MS, Tofwerk Inc.) was used to monitor the signal variations of TME and isoprene (Supplementary Fig. 9). Spectra were averaged every minute and analyzed using the Tofware package (version 3.2.5) in Igor Pro (Wavemetrics). The $^{\bullet}$OH radical concentration was calculated based on the below equation[69]:

$$[OH] = -\frac{\ln\left(\frac{ISO_t}{ISO_0}\right)}{tk} \qquad (1)$$

where k is the rate constant of the reaction between $^{\bullet}$OH and isoprene, ISO_t is the isoprene intensity at time t, and ISO_0 is the isoprene intensity prior to $^{\bullet}$OH oxidation.

Dark indoor experiments

The oxidation experiments involving organic films in the dark indoor environment were conducted in a desk drawer in an office of the Lash Miller Building at the University of Toronto. The room temperature was maintained between 22-25 °C. During the ML film oxidation experiment, the daily average outdoor ozone mixing ratio was approximately 31 ppb, while during the cooking oil oxidation experiment, the average ozone mixing ratio was around 25 ppb (data from local air quality monitor station: https://www.airqualityontario.com). Ozone measurements indicated that the indoor ozone concentration was about 70% of the outdoor levels, and the concentration in the dark drawer was approximately 67% of the indoor level.

Reactive oxygen species assays

In this study, reactive oxygen species (ROS) or organic hydroperoxides were quantified using the Ferrous Oxidation in Xylenol Orange version 2 (FOX2) and the 4-Nitrophenylboronic Acid (NPBA) assays. In the FOX2 assay, ROS oxidize Fe^{2+} to Fe^{3+}, which then forms a complex with xylenol orange, resulting in a color change[48,70]. This change is measured with a spectrophotometer at wavelengths of 560 nm or 600 nm. To prepare the FOX2 solution, 76 mg of xylenol orange tetrasodium salt and 98 mg of ammonium iron(II) sulfate hexahydrate were dissolved in 100 mL of 250 mM sulfuric acid. This solution was then mixed with 900 mL of peroxide-free methanol containing 1 g of BHT. For a measurement, 1 mL of FOX2 was added to 0.5 mL diluted extracts and allowed to react for 30 mins, after which the absorbance was measured using a UV-vis spectrometer (Ocean Optics USB2000 +). Due to its low detection limit for BHPO compared to the NPBA assay (Supplementary Fig. 4), the FOX2 assay was predominantly used in this study.

The NPBA assay is known for its sensitivity to H_2O_2 and organic hydroperoxides and can distinguish between these and organic peroxides (ROOR)[71]. In this assay, NPBA is oxidized by organic hydroperoxides to form 4-nitrophenol, which has a significant absorption at 406 nm[42]. For the assay, 0.5 ml of extracts were mixed with 2.0 mL of 1-propanol, 25 µL of NPBA (55 mM in methanol) and 225 µL KOH (275 mM) were incubated at 85 °C in a water bath for 2 h, after which the absorbance was measured.

Product measurement and identification

For mass spectral measurements of the products, the extracts were diluted tenfold with a mixture of 4 mM NH_4HCOO in methanol and 1-propanol (80:20 v/v). The diluted samples were then analyzed using a Thermo Q-Exactive Orbitrap high-resolution mass spectrometer (HRMS, Thermo Fisher Scientific) using heated electrospray ionization (ESI) in the positive mode. The HRMS, operating with a mass resolving power of 70,000 at *m/z* 200, covered a mass range from *m/z* 100 to 1500. Samples were directly injected into the HRMS at a flow rate of 15 µL min^{-1}. The analysis parameters for the ESI(+)-HRMS were as follows: spray voltage at 2.8 kV, sheath gas flow rate at 13 arbitrary units (arb. units), auxiliary gas flow rate at 0 arb. units, sweep gas flow at 0 arb. units and a capillary temperature of 220 °C.

Besides, the extracts were further analyzed using HRMS coupled with a Vanquish ultra-high-performance liquid chromatography (UHPLC) system (Thermo Fisher Scientific, USA). Separation was achieved with a C18 column (50 mm × 2.1 mm, 1.5 µm, Thermo Fisher Scientific, USA). The injection volume was 1 µL, and the mobile phases were 0.1% formic acid in water (solvent A) and 0.1% formic acid in methanol (solvent B). The flow rate was maintained at 0.25 mL min^{-1}. The gradient elution protocol was as follows: 5% B for 1.5 min, a linear gradient to 50% B over the next 2 min, then increasing to 100% B over the following 4 min, maintaining 100% B for another 3.5 min, returning to 5% B in 0.2 min, and finally holding at 5% B for 0.8 min. For HRMS analysis, a spray voltage of 3.25 kV was applied in positive ionization mode. The sheath gas flow rate was set to 30 arb. units, the auxiliary gas flow rate to 7 arb. units, and the sweep gas flow rate to 1 arb. units.

The capillary temperature was maintained at 350 °C. Data analysis was performed using Thermo Fisher Scientific FreeStyle 1.6.

For the identification of organic hydroperoxides, we utilized a refined direct infusion tandem mass spectrometry (MS/MS) method as previously described[27,38]. To confirm the structure of these compounds, a neutral loss scan of 51 Da ($H_2O_2 + NH_3$) was performed on the ammoniated ions $[M + NH_4]^+$ using ESI(+)-MS/MS. This method involved 0.5 mTorr Argon pressure and a collision-induced dissociation (CID) voltage of 25 V. Under these conditions, all signals displayed in the spectrum corresponded to the selected precursor (ROOH) ions prior to fragmentation.

In-film radical measurements

Hydroxyl radicals were detected using benzoic acid, a well-established $^{\bullet}$OH radical trap, resulting in similar percentages of product isomers (i.e., 2-, 3-, and 4-hydroxybenzoic acid)[50]. A 0.5 mL aliquot of benzoic acid (4 mM) in chloroform solution was added to both fresh and oxidized ML films. Following complete solvent evaporation, the coatings were placed back in either the dark drawer or flow reactor. After the reaction, 1 mL of methanol and then 0.5 mL of 1-propanol were used to extract the film. The extracts were further diluted with methanol and analyzed using UHPLC (Dionex, UltiMate 3000) coupled with a TSQ Endura Triple Quadrupole mass spectrometer (Thermo Scientific) in MRM mode. The gradient elution protocol was as follows: 5% B for 2 min, a linear gradient to 95% B in the next 8 min, 95% B for another 3 min, back to 5% B in 2 min, and then 5% B for 2 min. The flow rate was 0.25 mL min^{-1}. The C18 column (100 mm × 3 mm, 1.9 µm, Thermo Fisher Scientific, USA) was maintained at 40 °C. The settings for the ESI source were as follows: spray voltage at -2.5 kV, sheath gas flow rate at 20 arb. units, auxiliary gas flow rate at 3 arb. units, sweep gas flow rate at 1 arb. units, an ion transfer tube temperature of 350 °C and a vaporizer temperature of 150 °C.

Additionally, organic radicals formed in the ML films were detected using a Bruker CW X-band ECS-EMXplus EPR Spectrometer. Each ML coating was initially extracted with 1 mL chloroform containing 18 mM DMPO spin trap. Approximately 20 µL of this mixture was immediately transferred to a sealed capillary tube before being placed into the EPR resonator (ER4123D). All recorded spectra were referenced to 2,2-diphenyl-1-picrylhydrazyl (DPPH). The primary EPR settings were as follows: 9.34 GHz microwave frequency, 2.145 mW microwave power, 3332 G center field, 300 G sweep width, 50 dB receiver gain, 8 scans, 90 s sweep time, 30 ms conversion time, and 100 kHz modulation frequency with a modulation amplitude of 1 G. For radical speciation prediction, the experimental EPR spectrum was fitted using the WinSim software, and the hyperfine splitting constants were calculated accordingly[72].

Kinetics modeling

Kinetics modeling of the autoxidation process and fitting of this model to experimental data were accomplished using an in-house Python script provided in the SI which models concentration changes for reactions between methyl linolenate (RH as the abbreviation in the model), $^{\bullet}$OH, peroxy radicals ($RO_2^{\bullet}$), ROOH, and alkyl radical ($R^{\bullet}$). The model incorporated the reactions described in Fig. 4b. Due to the presence of two bis-allylic carbons and two less reactive allylic carbons in ML, initial RH concentration in the model is 3 times the concentration of ML present in the film. As shown in Fig. 4b, R_{init} is an arbitrary first-order initiation step (i.e., initiation by light or gas-phase $^{\bullet}$OH radicals), R1-R4 are propagation steps, R5 is the termination step, and R6 is an $^{\bullet}$OH sink representing OH radical reactions of the film.

The defined kinetic model behaves as a stiff differential equation system, so it was solved given inputs of each rate constant using the SciPy initial value problem solver 'solve_ivp'[73] using the fifth-order Radau IIA implicit Runge-Kutta method[74]. Based on expected concentrations of each species, a relative local error tolerance of 10^{-3} and absolute local error tolerances of 10^{-6}, 10^{-16}, 10^{-12}, 10^{-7}, and 10^{-12} for RH, $^{\bullet}$OH, $RO_2^{\bullet}$, ROOH, and $R^{\bullet}$ respectively were chosen. This solver outputs a full time series for each modeled species, and the time series for ROOH was fitted to experimental measurements of ROOH concentrations within the films by varying rate constants k_{init}, k_2, k_3, and k_5 using the SciPy 'curve_fit' function with the Trust Region Reflective algorithm[75] and a smooth approximation of the absolute value loss function ('soft_ l1'). Initial values of these rate constants for this algorithm were selected using the Differential Evolution optimization algorithm[76] set to minimize the root mean square error across the output time series. Bounds for this initial value selection were manually selected based on literature values[77] and resulting fit performance. Reported rate constants are best fit parameters based on this analysis for each dataset separately (Fig. 4). The initiation reaction R1 is treated as a pseudo first-order reaction, so the fit value for k_{init} incorporates the rate of initiating photolysis or gas-surface multiphase $^{\bullet}$OH chemistry, including the light intensity and gas-phase $^{\bullet}$OH concentration. The values of k_2 and k_5 are not expected to change between the dark drawer and $^{\bullet}$OH flow reactor experiments, so they were fit in the dark drawer experiment and then were fixed to those values when modeling the $^{\bullet}$OH flow reactor experiment. Finally, k_1 and k_4 are assumed to be fast (and the model is insensitive to changes in these variables) with values given in R1 and R4 (Fig. 4).

BPA oxidation product measurement

The procedure for adding BPA (4 mM in chloroform) to both fresh and oxidized films to react with $^{\bullet}$OH radicals, as well as the extraction method, was identical to the experiment involving the addition of BA solution. The extracts were subsequently diluted tenfold for UHPLC-HRMS analysis. The mobile phases consisted of (A) water and (B) methanol, with a flow rate of 0.25 mL min^{-1}. The gradient elution protocol settings were the same as previously described for product measurement. For HRMS analysis, a spray voltage of -3 kV was applied in negative ionization mode. The sheath gas flow rate was set to 35 arb. units, the auxiliary gas flow rate to 5 arb. units, and the sweep gas flow rate to 1 arb. units. The capillary temperature was maintained at 300 °C.

Data availability

All data are available in the main paper, the Supplementary Information files and from corresponding author upon request. Source data are provided with this paper.

Code availability

The code used for the model along with the data modeled here is provided in the Supplementary Information.

References

1. Girotti, A. W. Mechanisms of lipid peroxidation. *J. Free Radic. Biol. Med.* **1**, 87–95 (1985).
2. Crounse, J. D., Nielsen, L. B., Jørgensen, S., Kjaergaard, H. G. & Wennberg, P. O. Autoxidation of organic compounds in the atmosphere. *J. Phys. Chem. Lett.* **4**, 3513–3520 (2013).
3. Yin, H., Xu, L. & Porter, N. A. Free radical lipid peroxidation: mechanisms and analysis. *Chem. Rev.* **111**, 5944–5972 (2011).
4. Ehn, M. et al. A large source of low-volatility secondary organic aerosol. *Nature* **506**, 476–479 (2014).
5. Yu, H. et al. Atmospheric photo-oxidation of 2-ethoxyethanol: autoxidation chemistry of glycol ethers. *J. Phys. Chem. A* **127**, 9564–9579 (2023).
6. Mayorga, R., Xia, Y., Zhao, Z., Long, B. & Zhang, H. Peroxy radical autoxidation and sequential oxidation in organic nitrate formation during limonene nighttime oxidation. *Environ. Sci. Technol.* **56**, 15337–15346 (2022).

7. Bianchi, F. et al. Highly oxygenated organic molecules (HOM) from gas-phase autoxidation involving peroxy radicals: A key contributor to atmospheric aerosol. *Chem. Rev.* **119**, 3472–3509 (2019).
8. Guillen, M. D. & Goicoechea, E. Oxidation of corn oil at room temperature: primary and secondary oxidation products and determination of their concentration in the oil liquid matrix from 1H nuclear magnetic resonance data. *Food Chem.* **116**, 183–192 (2009).
9. Betteridge, D. J. What is oxidative stress? *Metabolism* **49**, 3–8 (2000).
10. Trachootham, D., Alexandre, J. & Huang, P. Targeting cancer cells by ROS-mediated mechanisms: a radical therapeutic approach? *Nat. Rev. Drug Discov.* **8**, 579–591 (2009).
11. Berliner, J. A. & Heinecke, J. W. The role of oxidized lipoproteins in atherogenesis. *Free Radic. Biol. Med.* **20**, 707–727 (1996).
12. Barnham, K. J., Masters, C. L. & Bush, A. I. Neurodegenerative diseases and oxidatives stress. *Nat. Rev. Drug Discov.* **3**, 205–214 (2004).
13. Ingold, K. U., Bowry, V. W., Stocker, R. & Walling, C. Autoxidation of lipids and antioxidation by α-tocopherol and ubiquinol in homogeneous solution and in aqueous dispersions of lipids: Unrecognized consequences of lipid particle size as exemplified by oxidation of human low density lipoprotein. *Proc. Natl Acad. Sci. USA.* **90**, 45–49 (1993).
14. Lim, C. Y. & Abbatt, J. P. Chemical composition, spatial homogeneity, and growth of indoor surface films. *Environ. Sci. Technol.* **54**, 14372–14379 (2020).
15. Larsson, K., Odham, G. & Södergren, A. On lipid surface films on the sea. I. a simple method for sampling and studies of composition. *Mar. Chem.* **2**, 49–57 (1974).
16. Carpenter, L. J. & Nightingale, P. D. Chemistry and release of gases from the surface ocean. *Chem. Rev.* **115**, 4015–4034 (2015).
17. Eglinton, G. & Hamilton, R. J. Leaf epicuticular waxes: The waxy outer surfaces of most plants display a wide diversity of fine structure and chemical constituents. *Sci. (80).* **156**, 1322–1335 (1967).
18. Dinel, H., Schnitzer, M. & Mehuys, G. R. Soil lipids: origin, nature, content, decomposition, and effect on soil physical properties. *Soil Biochem.* **6**, 397–429 (2017).
19. Deming, B. L. & Ziemann, P. J. Quantification of alkenes on indoor surfaces and implications for chemical sources and sinks. *Indoor Air* **30**, 914–924 (2020).
20. Weschler, C. J. & Nazaroff, W. W. Growth of organic films on indoor surfaces. *Indoor Air* **27**, 1101–1112 (2017).
21. Liu, Q. T., Chen, R., McCarry, B. E., Diamond, M. L. & Bahavar, B. Characterization of polar organic compounds in the organic film on indoor and outdoor glass windows. *Environ. Sci. Technol.* **37**, 2340–2349 (2003).
22. Li, M., Butka, E. & Wang, X. Comprehensive quantification of triacylglycerols in soybean seeds by electrospray ionization mass spectrometry with multiple neutral loss scans. *Sci. Rep.* **4**, 1–11 (2014).
23. Andrikopoulos, N. K. Triglyceride species compositions of common edible vegetable oils and methods used for their identification and quantification. *Food Rev. Int.* **18**, 71–102 (2002).
24. Weschler, C. J. & Nazaroff, W. W. Human skin oil: a major ozone reactant indoors. *Environ. Sci. Atmos.* **3**, 640–661 (2023).
25. Nicolaides, N. Skin lipids: their biochemical uniqueness. *Sci. (80).* **186**, 19–26 (1974).
26. Wisthaler, A. & Weschler, C. J. Reactions of ozone with human skin lipids: Sources of carbonyls, dicarbonyls, and hydroxycarbonyls in indoor air. *Proc. Natl Acad. Sci. USA.* **107**, 6568–6575 (2010).
27. Zhou, Z., Crilley, L. R., Ditto, J. C., VandenBoer, T. C. & Abbatt, J. P. D. Chemical fate of oils on indoor surfaces: Ozonolysis and peroxidation. *Environ. Sci. Technol.* **57**, 15546–15557 (2023).
28. Zhou, Z. et al. Multiphase ozonolysis of oleic acid-based lipids: quantitation of major products and kinetic multilayer modeling. *Environ. Sci. Technol.* **56**, 7716–7728 (2022).
29. Müller, M. et al. Electrodynamic balance-mass spectrometry reveals impact of oxidant concentration on product composition in the ozonolysis of oleic acid. *Phys. Chem. Chem. Phys.* **41**, 27086–27104 (2022).
30. Zahardis, J. & Petrucci, G. A. The oleic acid-ozone heterogeneous reaction system: products, kinetics, secondary chemistry, and atmospheric implications of a model system - a review. *Atmos. Chem. Phys.* **7**, 1237–1274 (2007).
31. Paquette, G., Kupranycz, D. B. & van de Voort, F. R. The Mechanisms of lipid autoxidation I. primary oxidation products. *Can. Inst. Food Sci. Technol. J.* **18**, 112–118 (1985).
32. Frankel, E. N. et al. Hydroperoxide formation. *Lipid Oxid.* 25–50 https://doi.org/10.1533/9780857097927.25 (2012).
33. Zeng, M. & Wilson, K. R. Evaluating possible formation mechanisms of criegee intermediates during the heterogeneous autoxidation of squalene. *Environ. Sci. Technol.* **58**, 11587–11595 (2024).
34. Zeng, M., Heine, N. & Wilson, K. R. Evidence that criegee intermediates drive autoxidation in unsaturated lipids. *Proc. Natl Acad. Sci. USA.* **117**, 4486–4490 (2020).
35. Li, L., Arnot, J. A. & Wania, F. How are humans exposed to organic chemicals released to indoor air? *Environ. Sci. Technol.* **53**, 11276–11284 (2019).
36. Eichler, C. M. A. et al. Assessing human exposure to SVOCs in materials, products, and articles: a modular mechanistic framework. *Environ. Sci. Technol.* **55**, 25–43 (2021).
37. Porter, N. A., Weber, B. A., Weenen, H. & Khan, J. A. Autoxidation of polyunsaturated lipids. factors controlling the stereochemistry of product hydroperoxides. *J. Am. Chem. Soc.* **102**, 5597–5601 (1980).
38. Zhou, S., Rivera-Rios, J. C., Keutsch, F. N. & Abbatt, J. P. D. Identification of organic hydroperoxides and peroxy acids using atmospheric pressure chemical ionization-tandem mass spectrometry (APCI-MS/MS): Application to secondary organic aerosol. *Atmos. Meas. Tech.* **11**, 3081–3089 (2018).
39. Abbatt, J. P. D. & Wang, C. The atmospheric chemistry of indoor environments. *Environ. Sci. Process. Impacts* **22**, 25–48 (2020).
40. Su, G., Wei, Y. & Guo, M. Direct colorimetric detection of hydrogen peroxide using 4-nitrophenyl boronic acid or its pinacol ester. *Am. J. Anal. Chem.* **02**, 879–884 (2011).
41. Wang, S. et al. Organic peroxides in aerosol: Key reactive intermediates for multiphase processes in the atmosphere. *Chem. Rev.* https://doi.org/10.1021/acs.chemrev.2c00430 (2022).
42. Jiang, H., Jang, M. & Yu, Z. Dithiothreitol activity by particulate oxidizers of SOA produced from photooxidation of hydrocarbons under varied NOx levels. *Atmos. Chem. Phys.* **17**, 9965–9977 (2017).
43. Chan, H. W. S. & Levett, G. Autoxidation of methyl linolenate: Analysis of methyl hydroxylinolenate isomers by high performance liquid chromatography. *Lipids* **12**, 837–840 (1977).
44. Brash, A. R. Autoxidation of methyl linoleate: Identification of the bis-allylic 11-hydroperoxide. *Lipids* **35**, 947–952 (2000).
45. Choe, E. & Min, D. B. Mechanisms and factors for edible oil oxidation. *Compr. Rev. Food Sci. Food Saf.* **5**, 169–186 (2006).
46. Zhou, Z., Zhou, S. & Abbatt, J. P. D. Kinetics and condensed-phase products in multiphase ozonolysis of an unsaturated triglyceride. *Environ. Sci. Technol.* **53**, 12467–12475 (2019).
47. Hartwig, C. L. et al. Investigating the antimalarial action of 1,2,4-trioxolanes with fluorescent chemical probes. *J. Med. Chem.* **54**, 8207–8213 (2011).
48. Morrison, G., Moravec, R. & Yao, Z. Ozone-initiated yield of reactive oxygen species in a model indoor surface film. *Environ. Sci. Technol. Lett.* **10**, 528–532 (2023).

49. Jankowski, J. J., Kieber, D. J. & Mopper, K. Nitrate and nitrite ultraviolet actinometers. *Photochem. Photobiol.* **70**, 319–328 (1999).
50. Zhou, X. & Mopper, K. Determination of photochemically produced hydroxyl radicals in seawater and freshwater. *Mar. Chem.* **30**, 71–88 (1990).
51. Tong, H. et al. Hydroxyl radicals from secondary organic aerosol decomposition in water. *Atmos. Chem. Phys.* **16**, 1761–1771 (2016).
52. Gerritz, L. et al. Reactive oxygen species formation and peroxide and carbonyl decomposition in aqueous photolysis of secondary organic aerosols. *Environ. Sci. Technol.* **58**, 4716–4726 (2024).
53. Drouza, C., DIeronitou, A., Hadjiadamou, I. & Stylianou, M. Investigation of phenols activity in early stage oxidation of edible oils by electron paramagnetic resonance and 19F NMR spectroscopies using novel lipid vanadium complexes as radical initiators. *J. Agric. Food Chem.* **65**, 4942–4951 (2017).
54. Liu, Y., Wang, Y., Cao, P. & Liu, Y. Combination of gas chromatography-mass spectrometry and electron spin resonance spectroscopy for analysis of oxidative stability in soybean oil during deep-frying process. *Food Anal. Methods* **11**, 1485–1492 (2018).
55. Weschler, C. J. & Shields, H. C. Production of the hydroxyl radical in indoor air. *Environ. Sci. Technol.* **30**, 3250–3258 (1996).
56. White, I. R. et al. Use of reactive tracers to determine ambient OH radical concentrations: Application within the indoor environment. *Environ. Sci. Technol.* **44**, 6269–6274 (2010).
57. Singer, B. C. et al. Indoor secondary pollutants from cleaning product and air freshener use in the presence of ozone. *Atmos. Environ.* **40**, 6696–6710 (2006).
58. Weschler, C. J. Ozone in indoor environments: concentration and chemistry. *Indoor Air* **10**, 269–288 (2000).
59. Morrison, G. C. et al. Partitioning of reactive oxygen species from indoor surfaces to indoor aerosols. *Environ. Sci. Process. Impacts* **24**, 2310–2323 (2022).
60. Hoekstra, E. J. & Simoneau, C. Release of bisphenol A from polycarbonate-A review. *Crit. Rev. Food Sci. Nutr.* **53**, 386–402 (2013).
61. Fonseca, M. I., Lorigo, M. & Cairrao, E. Endocrine-disrupting effects of bisphenol A on the cardiovascular system: A review. *J. Xenobiotics* **12**, 181–213 (2022).
62. Rubin, B. S. Bisphenol A: an endocrine disruptor with widespread exposure and multiple effects. *J. Steroid Biochem. Mol. Biol.* **127**, 27–34 (2011).
63. Xiao, Y. et al. Roles of hydroxyl and carbonate radicals in bisphenol a degradation via a nanoscale zero-valent iron/percarbonate system: influencing factors and mechanisms. *RSC Adv.* **11**, 3636–3644 (2021).
64. Han, Q. et al. Effectiveness and degradation pathways of bisphenol A (BPA) initiated by hydroxyl radicals and sulfate radicals in water: Initial reaction sites based on DFT prediction. *Environ. Res.* **216**, 1–10 (2023).
65. Nakagawa, Y. & Suzuki, T. Metabolism of bisphenol A in isolated rat hepatocytes and oestrogenic activity of a hydroxylated metabolite in MCF-7 human breast cancer cells. *Xenobiotica* **31**, 113–123 (2001).
66. Kitamura, S. et al. Comparative study of the endocrine-disrupting activity of bisphenol A and 19 related compounds. *Toxicol. Sci.* **84**, 249–259 (2005).
67. Huang, D. D. et al. Comparative assessment of cooking emission contributions to urban organic aerosol using online molecular tracers and aerosol mass spectrometry measurements. *Environ. Sci. Technol.* **55**, 14526–14535 (2021).
68. Li, R. et al. Source apportionment of PM2.5 in Shanghai based on hourly organic molecular markers and other source tracers. *Atmos. Chem. Phys.* **20**, 12047–12061 (2020).
69. Alwarda, R., Zhou, S. & Abbatt, J. P. D. Heterogeneous oxidation of indoor surfaces by gas-phase hydroxyl radicals. *Indoor Air* **28**, 655–664 (2018).
70. Nourooz-Zadeh, J. Ferrous ion oxidation in presence of xylenol orange for detection of lipid hydroperoxides in plasma. *Methods Enzymol.* **300**, 58–62 (1999).
71. Zhang, W., Zhao, Z., Shen, C. & Zhang, H. Unexpectedly efficient aging of organic aerosols mediated by autoxidation. *Environ. Sci. Technol.* **57**, 6965–6974 (2023).
72. Xie, L. N. et al. An unusual double radical homolysis mechanism for the unexpected activation of the aldoxime nerve-agent antidotes by polyhalogenated quinoid carcinogens under normal physiological conditions. *Free Radic. Biol. Med.* **130**, 1–7 (2019).
73. Virtanen, P. et al. SciPy 1.0: fundamental algorithms for scientific computing in Python. *Nat. Methods* **17**, 261–272 (2020).
74. Butcher, J. C. Integration processes based on radau quadrature formulas. *Math. Comput.* **18**, 233 (1964).
75. Branch, M. A., Coleman, T. F. & Li, Y. A subspace, interior, and conjugate gradient method for large-scale bound-constrained minimization problems. *SIAM J. Sci. Comput.* **21**, 1–23 (1999).
76. Storn, R. & Price, K. Differential evolution–a simple and efficient heuristic for global optimization over continuous spaces. *J. Glob. Optim.* **11**, 341–359 (1997).
77. Howard, J. A. & Ingold, K. U. Absolute rate constants for hydrocarbon autoxidation. VI. alkyl aromatic and olefinic hydrocarbons. *Can. J. Chem.* **45**, 793–802 (1967).
78. Babić, N., Pondaven, S. & Vezin, H. EPR spin-trapping study of free radical intermediates in polyalphaolefin base oil autoxidation. *Polym. Degrad. Stab.* **192**, 109687 (2021).
79. Dikalov, S. I. & Mason, R. P. Spin trapping of polyunsaturated fatty acid-derived peroxyl radicals: reassignment to alkoxyl radical adducts. *Free Radic. Biol. Med.* **30**, 187–197 (2001).

Acknowledgements

The authors acknowledge the financial support of NSERC Canada (RGPIN-2023-03326 to J.P.D.A) and helpful discussions with Dr. Zilin Zhou.

Author contributions

X.W. and J.P.D.A. designed the research project. X.W. performed the experiments. X.W., L.X., and H.P. analyzed data. W.F. and J.P.D.A. did the kinetic modeling. X.W. and J.P.D.A. wrote the paper.

Competing interests

The authors declare no competing interests.

Additional information

Supplementary information The online version contains supplementary material available at https://doi.org/10.1038/s41467-025-56802-0.

Correspondence and requests for materials should be addressed to Jonathan P. D. Abbatt.

Peer review information *Nature Communications* thanks Charles J. Weschler and the other, anonymous, reviewer(s) for their contribution to the peer review of this work. A peer review file is available.